Influence of weave architecture on mechanical response of SiC$_f$-SiC$_m$ tubular composites

James Nance [a], Ghatu Subhash [b,*], Bhavani Sankar [b], Nam-Ho Kim [b], Christian Deck [c], Sarah Oswald [c]

[a] *Department of Material Science and Engineering, University of Florida, Gainesville, FL 32611, USA*
[b] *Department of Mechanical and Aerospace Engineering, University of Florida, Gainesville, FL 32611, USA*
[c] *General Atomics, San Diego, CA 92121, USA*

ABSTRACT

Due to their high resistance to radiation damage and elevated temperature, silicon carbide fiber-reinforced, silicon carbide matrix composites (SiC$_f$-SiC$_m$) are identified as potential cladding structures for use in nuclear reactors. In this study, four composite architectures with varying ply numbers along the thickness direction and different biaxial or triaxial plain weave orientations at either 45° or 60°, were systematically evaluated under various stress states to assess the influence of weave architecture on mechanical performance. Experiments were conducted on SiC$_f$-SiC$_m$ composite tubes under tensile hoop, axial compression, and rotating flexural loading to evaluate the mechanical response and investigate the failure modes using high-speed imaging and digital image correlation (DIC) techniques. It was found that for tensile hoop burst and flexural loading, the braiding angle had the most significant influence on the strength of the composite, whereas the effect of fiber angle was more limited for compression testing. Under axial compression a unique failure mode where a microcrack nucleates and grows only to a length equal to the thickness of a single yarn was identified. This crack growth behavior is reflected as periodic oscillations in the load-displacement response. For both axial and hoop loading, regardless of weave angle and number of plies, failure always initiated parallel to the tube axis in a single yarn and the cumulative interaction of these microcracks lead to either axial burst or fracture at an angle to the tube axis along a yarn. These results point to the importance of customizing the design of tube architecture for enhanced performance in specified nuclear applications.

1. Introduction

Silicon carbide (SiC) is a structural ceramic with applications for high-temperature and extreme radiation environments and has been recognized as a potential candidate for cladding in the Accident Tolerant Fuel (ATF) systems [1–3]. To improve the toughness of SiC for nuclear applications, continuous SiC fiber-reinforced SiC matrix (SiC$_f$-SiC$_m$) composites have been developed which offer significant advantages over their monolithic counterparts. These advantages include a pseudo-ductile failure mode in the form of crack deflection and crack bridging, as well as tailorable physical and mechanical properties [4]. These SiC$_f$-SiC$_m$ composites are manufactured through various fabrication processes such as melt infiltration, polymer infiltration and pyrolysis, nano-powder infiltration and transient eutectoid process, and chemical vapor infiltration (CVI) [5–8]. In particular, CVI has shown the

most promise because it produces a high purity, highly crystalline β-SiC in the matrix phase, which has also been found to have high radiation resistance in nuclear environments [8].

For the successful implementation of components made of these SiC$_f$-SiC$_m$ composites in nuclear reactors, it is necessary to understand their mechanical response under a variety of loading conditions. In recent years, a large effort has been aimed towards understanding the stress-strain response of SiC$_f$-SiC$_m$ tubular composites under a variety of loading conditions. Jacobsen et al. performed a comparison study between the C-ring test and an expanding plug test to determine the tensile hoop strength of SiC$_f$-SiC$_m$ tubular composites [9]. In this study, the authors describe the stress-strain response of the composite during the loading of the tensile hoop burst specimen. The composite experienced an initial linear region until the onset of matrix cracking occurs at the proportional limit stress, at which point a pseudo-ductile like behavior is

exhibited until the ultimate failure. Bumgardner et al. monitored the fracture behavior of SiC_f-SiC_m composites during a 4-point bending test using acoustic emissions and measured spatial strains at fracture events such as matrix cracking and eventual loss of load-bearing capability [10]. It was found that there are four distinct stages of damage evolution during flexural loading: (1) matrix crack initiation; (2) loss of hermeticity; (3) fiber fracture followed by matrix crack widening; and (4) tow failure and loss of load-bearing capability. Rohmer et al. performed axial and hoop tensile tests on tubular SiC_f-SiC_m composites and revealed progressive loss in stiffness upon load exceeding the proportional limit but little permanent deformation upon unloading due to matrix and delamination cracks [11]. Lastly, Shapovalov et al., reported the mechanical strength of axial-biased reinforced SiC_f-SiC_m composites under uniaxial and biaxial stress states. For this study, the SiC_f-SiC_m composites tested had an axial-biased architecture, however, the hoop strength was observed to be higher than the axial strength. This suggested a complex role of the anisotropy of the composite on the strength and failure behavior [12].

However, the above body of work is still limited in its scope and most studies only focused on the mechanical response of a single architecture. A more complete understanding of the response of SiC_f-SiC_m composites under different loading conditions would provide a significant benefit for designers of composite parts for specific applications. For example, these effects would include the influence of composite architecture (e.g., number of plies in the thickness direction, the orientation of yarn and weave patterns, etc.) on various failure modes in the hoop, bending and axial directions. In contrast to more commercially established composite materials (such as carbon fiber-reinforced composites for aerospace), the understanding for SiC_f-SiC_m composites is limited. To fill this gap, we have conducted a suite of quasi-static axial compression, hoop tensile burst, and rotating flexural tests on composites with different architectures and number of plies. The aim is to understand and compare the failure mechanisms and strength dependence as a function of loading type and tube architecture, and in doing so, provide a more thorough understanding for designers of SiC_f-SiC_m composites to tailor performance for specific applications.

2. Experimental

The SiC_f-SiC_m composite tubes used in this study were manufactured by General Atomics Electromagnetic Systems (San Diego, CA, USA). Hi-Nicalon Type-S SiC fibers were used to create various reinforcement structures with plain-woven architectures, as defined by the test matrix. The fibers were bundled into yarns, each consisting of approximately 500 filaments, and woven into the desired architectures to create the fibrous preform which was then placed into a coating reactor, where each filament is individually coated with approximately 500 nm thick pyrolytic carbon (PyC). The fibrous preform was then densified, via CVI, with β-SiC matrix. Tubes with four different architectures were manufactured to study the effects of architecture and number of plies on the mechanical properties: (1) biaxial 45° plain-woven 2-ply, (2) biaxial 45° plain-woven 3-ply, (3) biaxial 60° (hoop-biased) plain-woven 2-ply, and (4) triaxial 45° 2-ply braided. Optical images of these tube architectures are shown in Fig. 1. The unit cell for each architecture is outlined in red. For the biaxial architectures, the unit cell consists of two overlapping yarns oriented at the stated angle. For the triaxial architecture, an additional axial yarn bisects the biaxial yarns. Note that for the 45° biaxial composite, a 2-ply or 3-ply configuration in the thickness direction is achieved by weaving additional layers of the composite over the first ply. Each specimen had approximately 30–40% fiber volume fraction throughout the composite. The tube dimensions of each architecture are summarized in Table 1.

The performance of the above composite architectures was evaluated under three loading conditions: (i) quasistatic axial compression, (ii) tensile hoop, and (iii) rotating flexure. For each type of test, the length of the composite specimen varied. In the following sections, the details of the test procedure are presented.
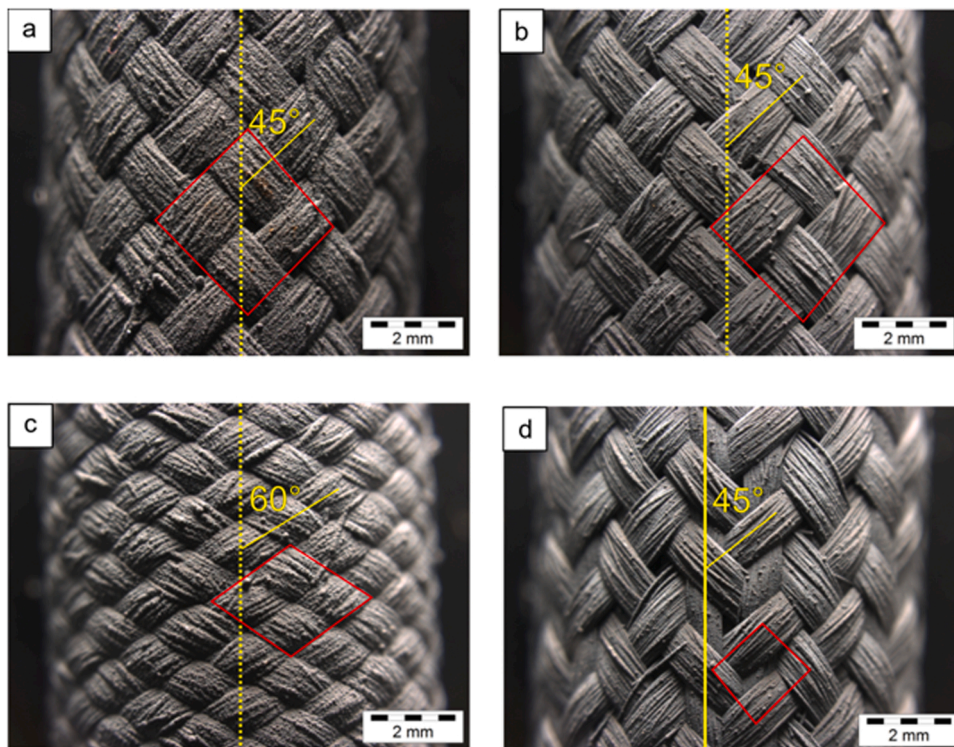
Fig. 1. SiC_f-SiC_m tubular composite architectures. The dashed line represents the vertical axis and the solid lines represent the yarn orientation. The red outline is the unit cell. (a) 45° 2-ply biaxial; (b) 45° 3-ply biaxial; (c) 60° 2-ply biaxial (hoop biased); and (d) 45° 2-ply triaxial.

Table 1
Dimensions of SiC$_f$-SiC$_m$ composite tube for each architecture.

| Parameter	45° 2-ply biaxial	45° 3-ply biaxial	60° 2-ply biaxial	45° 2-ply triaxial
Inner diameter	7.8 ± 0.2 mm	7.8 ± 0.2 mm	7.8 ± 0.2 mm	7.8 ± 0.2 mm
Outer diameter	9.31 ± 0.4 mm	9.63 ± 0.4 mm	9.38 ± 0.4 mm	9.47 ± 0.4 mm
Thickness	0.76 mm	0.92 mm	0.79 mm	0.84 mm

2.1. Quasistatic axial compression test

Axial compression testing was performed using the guidelines present in ASTM C1424 [13] on specimens of length 14.3 mm of all four architectures at room temperature (25 °C) and in atmospheric conditions. A series of 10 tests per architecture was conducted. The compression test specimens were cut out from longer lengths of fabricated tubes. The cutting process can introduce defects on the cut surfaces (e.g., minor chipping of the fibers and the matrix, microcracks) and these defects act as sources for premature fracture during load application. In an attempt to minimize these edge effects during axial loading, a layer of compliant Grafoil®, 0.5 mm thick, was placed between the sample and the loading platens. This Grafoil® is expected to fill in the small gaps between the contacting surfaces and reduce the stress concentrations [14] and potential premature crack initiation from the defects during the early part of load application. Compression tests were carried out in a TestResources® 315–150 frame universal testing machine. A camera was mounted in front of the specimen to capture the failure mode during deformation.

While the above specimen length provided overall deformation behavior, it was later found that more insight into the mechanism for failure propagation can be gained by conducting compression tests on specimens of length with a different number of unit cells of the composites (specimens that were longer or shorter). From a single 45° 2-ply architecture, samples were cut in lengths corresponding to 1, 2, 4, and 8-unit cells (2.30 mm, 4.60 mm, 10.40 mm, and 18.40 mm, respectively). Due to the high material and specimen preparation costs, such tests were carried out on only this one architecture. We anticipate a similar deformation behavior in other architectures as well.

2.2. Tensile hoop burst test

Temperature gradients, cladding swelling, and fuel swelling during nuclear reactor operation can induce significant hoop stress in the cladding [15]. For example, temperature-dependent swelling in SiC and SiC$_f$-SiC$_m$ composites, coupled with cladding through-thickness thermal gradients can lead to complex stress states [16,17]. Fission gas formation can build up internal pressure. During a power ramp in the reactor, the ceramic fuel expands and the fuel begins to crack from the center of the fuel pellet to the outer surface. This fuel swelling can close the fuel-cladding gap and impose fuel-cladding mechanical interaction stresses on the cladding. Therefore, the determination of hoop stress of the SiC$_f$-SiC$_m$ composite tubes is of practical relevance. All the chosen architectures were tested in hoop tensile mode according to ASTM C1819 at room temperature [18]. The schematic of the setup used for the hoop strength test is shown in Fig. 2.

The tubular specimens were cut to approximately 63 mm in length. An 18.5 mm tall polyurethane plug of 95A durometer (McMaster-Carr 8784K15) was inserted into the tube to induce uniform hoop stress on the composite. The plug was machine cut to be a snug fit inside the tube and the cylindrical surfaces were lubricated with Teflon spray for easy insertion and to reduce frictional effects during loading. The polymer plug was pushed to the central portion of the tube length and compressed on either side by metallic pushrods in an Instron machine with a 50 kN load cell. A crosshead speed of 3 mm/min was used. As the plug is
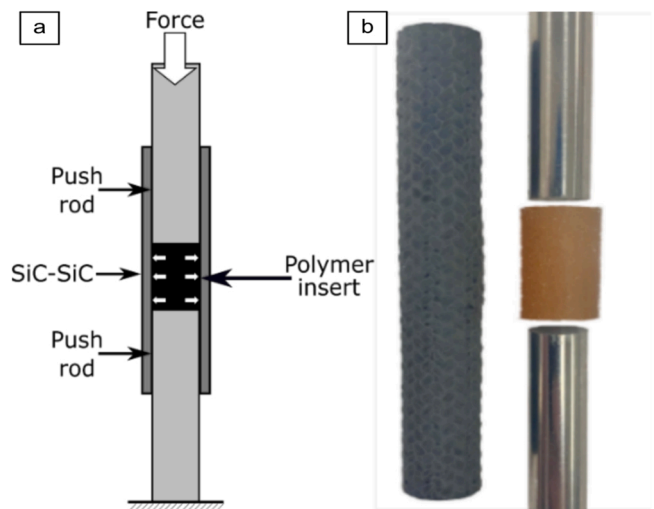
Fig. 2. Tensile hoop burst test configuration. (a) Illustration of the test configuration and (b) Composite specimen, elastomeric insert, and metallic pushrods.

compressed, the elastomer expands radially and exerts a uniform radial pressure on the inner surface of the tube. However, the stress varies through the thickness of the composite from the inner diameter to the outer diameter. Mosley [19] showed that the hoop stress at the outer diameter could be calculated from

$$\sigma_\theta = \eta P \frac{2r_i^2}{[r_o^2 - r_i^2]} \tag{1}$$

where η is the maximum stress factor (1.05 for the outer diameter) [18]; r_i is the inner radius of the tube (mm); r_o is the outer radius of the tube (mm); P is the internal pressure (MPa) exerted on the tubular composite by the polymer plug, given by:

$$P = \frac{F}{\pi r_i^2} \tag{2}$$

To account for the axial load taken up by the plug and the pushrods, the plug was separately compressed (with no tube surrounding it) to the same displacement as in the hoop test. This load is then subtracted from the failure load of the hoop test on the composite specimen. A high-speed video camera (Phantom v710, Vision Research, Inc., Way) was used to capture the failure mode of the composites at 120,000 frames per second with a resolution of approximately 128 × 256 pixels.

Furthermore, to verify that uniform hoop stress is induced on the surface of the composite during the loading process, the hoop displacement was tracked in each test. Due to the high surface undulations resulting from the braiding process, conventional methods such as bonded strain gages could not be used to measure surface strains. Instead, digital image correlation (DIC) was employed to measure the surface displacement by stereo correlation of images from two cameras (Point Grey Research, Inc. FL2–20S4M-C) orientated at an in-plane angle of approximately 22.5°. The cameras were calibrated with 30 images of a standard calibration grid from Correlated Solutions, Inc. The calibration procedure consisted of moving, imaging, and analyzing the calibration grid in front of the pair of cameras at various positions to calibrate both the intrinsic parameters (i.e., image scale, focal length, lens distortions, etc.) and extrinsic parameters (i.e., stereo-angle, distance between cameras, distance from cameras to sample, etc.). Then the outer surface of the composites was sprayed with black and white spray paints to create a speckle pattern. During the application of the load, the relative displacement of the speckles was imaged (one image every three seconds) as the specimen undergoes deformation, and the strain field was extracted [20,21]. The captured images were analyzed using

Vic3D® (Correlated Solutions Inc.) software, which provided the hoop strain distribution on the specimen gage section surface.

2.3. Flexural testing

The flexural strength of the SiC$_f$-SiC$_m$ tubular composites was measured using a novel rotating four-point bend fixture. In the conventional static four-point flexure testing, only one side of the test specimen is exposed to the tensile stress. In a heterogeneous composite, with the random distribution of flaws throughout the specimen, there is a strong likelihood that the critical flaw may not lie on a plane with the maximum tensile stress during the bend test. Hence, only those flaws that exist on the tensile surface will be activated to propagate into larger cracks and induce failure. Therefore, if the critical flaw lies on the compression side of the test specimen during the static four-point flexure test, it will not be activated and the resulting strength of the material will be higher than the "true" flexural strength.

To remedy this situation and ensure that all the surface defects are exposed to the tensile stress and thereby measure the "true" flexural strength of the material, a novel test fixture was designed to rotate the specimen while simultaneously applying the flexural load. An image of the fixture and the test setup mounted in an Instron test machine are shown in Fig. 3. The test fixture consists of a lower assembly for support and to rotate the specimen, and an upper assembly to apply load to the specimen. Each assembly houses two sets of rollers mounted on four separate cylindrical shafts. The specimen is placed between these four pairs of rollers. The distance between the two lower rollers is approximately 120 mm, while the distance between the two upper rollers is approximately 40 mm. One of the bottom shafts is connected through a gearbox (AutomationDirect, Inc. model PGCN23–2525) to an encoded

Fig. 3. Rotating flexural test setup to determine the flexural strength of ceramic matrix composite tubes [21].

servo motor (Teknic, Inc., model CPM-MCVC-2311 S-RQN) and acts as a driveshaft to rotate two rollers that are in contact with the specimen. The rest of the shafts and rollers can only rotate by frictional contact with the cylindrical specimen. The fixture was validated on brittle glass rods with different surface treatments and 3D printed tubes. A more detailed discussion and validation of the rotating flexural test can be found in MacIsaac, et. al [22]. The flexural strength of the tubular composite can be calculated using the following equation:

$$\sigma_f = \frac{P_{max}(L_o - L_i)r_o}{4\left[\frac{\pi(r_o^4 - r_i^4)}{4}\right]} \tag{3}$$

where P_{max} is the load at failure; L_o is the distance between the outer anvils (mm); L_i is the distance between the inner anvils (mm). All of the composite flexural specimens used in this investigation were nominally 150 mm in length. The rotational speed of the specimen was set at 120 RPM and was monitored throughout the test duration. This speed was chosen to minimize the torque induced on the specimen while simultaneously providing sufficient friction between the specimen and the rollers for continuous rotation of the specimen. When the desired speed reached this threshold, load was applied on the specimen via the Instron machine at a displacement rate of 0.0043 mm/s until fracture occurred, which took approximately 2 min.

3. Results and discussion

3.1. Quasistatic compression

The measured failure strength values of the quasi-static axial compression tests are summarized in Table 2. During these tests, the specimens were observed to fail at two distinct locations, as illustrated in Fig. 4: (1) failure in the vicinity of the loading surface and (2) failure away from the loading surface, i.e., within the mid-section (or gage section) of the specimen. The only architecture that did not reveal both failure modes was the 45° 2-ply triaxial braided tube, which only failed at the loading edge of the specimens. The effects of edges and edge thickness on the failure of composite has been reported previously by Owens et al. [23]. Despite the use of the Grafoil® layer between the sample and the platens, failure did occur along the cut surfaces. These specimens exhibited significantly lower strength compared to the specimens that failed in the gage section (see Table 2). This premature failure along the edges seems to stem from the defects induced during the cutting and subsequent polishing of the cut surfaces of the test specimens. The cutting process of the tubes induce defects (cracks) in between the yarns, and in between the fibers within the yarns as they separate due to applied shear forces. Loss of matrix material around the fibers and the yarns also induces additional defects. All these defects can cause premature fracture along the edges of the specimen during loading. However, if the quality of the cut surface is good, the specimen failure can occur in the gage section. Interestingly, the 45° 2-ply triaxial
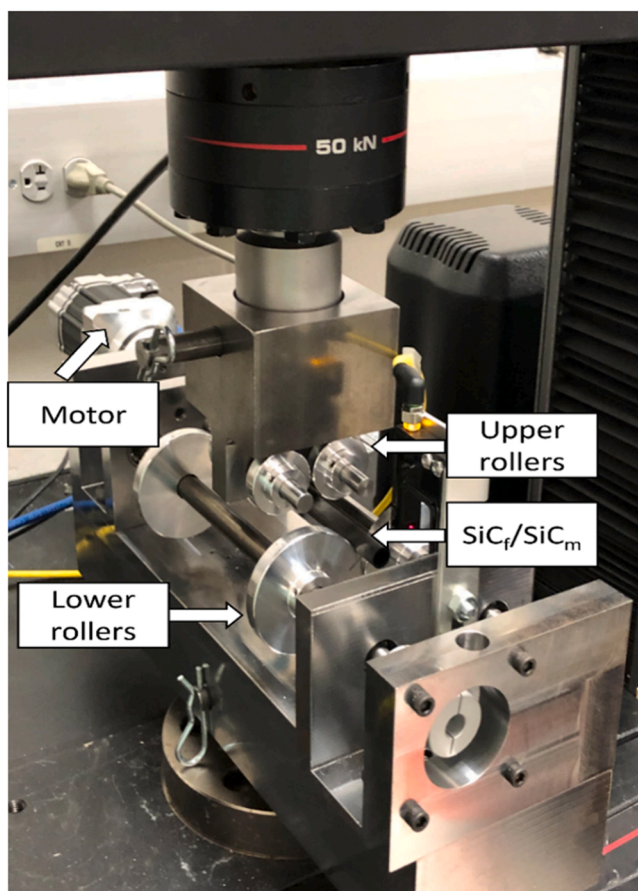
Table 2
Quasistatic axial compression strength values for various composite architectures.

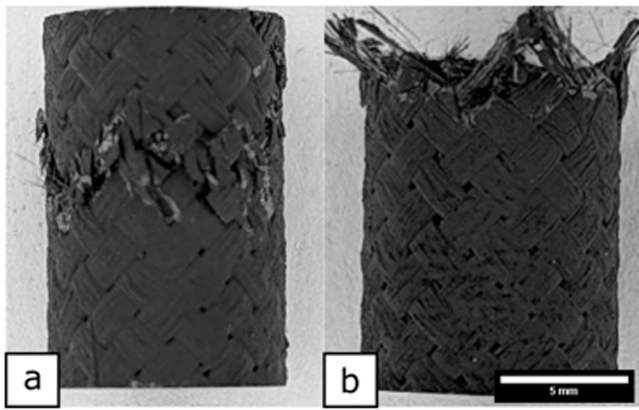| Architecture	Failure at edge		Failure in gage section	
	Strength (MPa)	Number of tests	Strength (MPa)	Number of tests
45° 2-ply biaxial	64.04 ± 2.89	5	97.46 ± 2.63	5
45° 3-ply biaxial	80.76	1	101.59 ± 8.12	9
60° 2-ply biaxial	62.53 ± 1.46	7	73.65 ± 4.22	3
45° 2-ply triaxial	65.72 ± 11.26	10	N/a	0

Fig. 4. Failure modes of SiC$_f$-SiC$_m$ composites during quasistatic axial compression. (a) Gage section failure (away from the specimen edge) and (b) loading edge failure.

composite specimens failed only along the edges, and none of the test specimens showed gage section failure (see Table 2). This result implies that for specimens with a higher number of yarn orientations in the composite it is difficult to polish the cut surfaces without inducing defects. Yarn orientations is defined as the number of yarns biased in the direction of interest, in this case the cutting surface. Therefore, the true failure strength is expected to be higher than the values shown in Table 2.

It is also noted from Table 2 that there is no significant difference in the strength of the composite tubes between the four tested architectures. There is a slight increase in strength of the two 45° biaxial architectures compared to the 60° architecture, probably due to a higher axial bias of the 45° yarns to the applied load. Overall, these results indicate that there is no significant influence of weave architecture on the compressive mechanical response. A similar trend is observed even for the edge fractured specimens where all architectures failed at a similar value of approximately 65 MPa (discounting the single data of the 45° 3-ply composite).

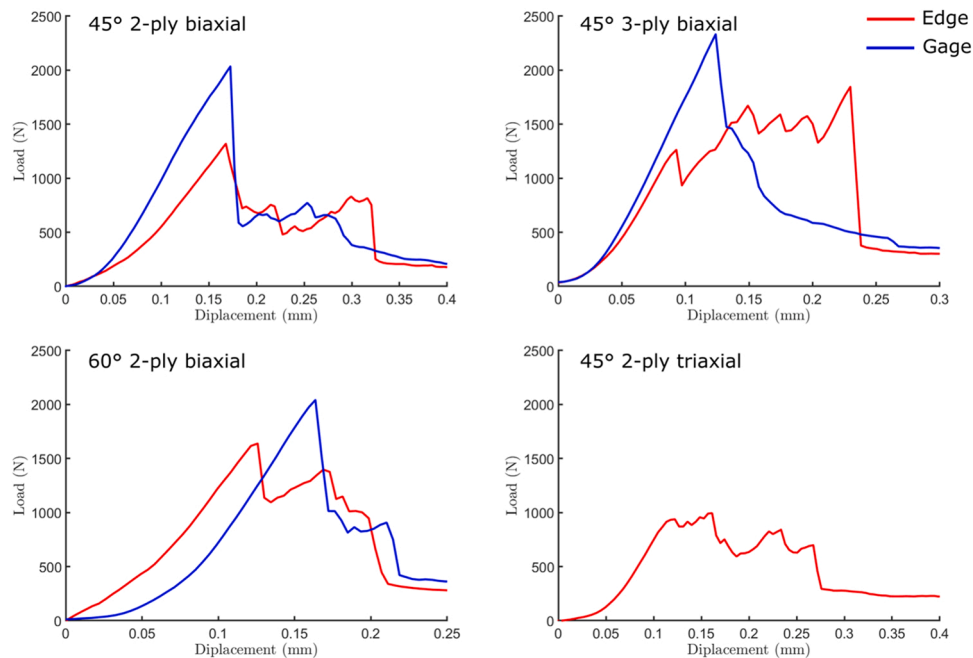The characteristic load-displacement curves for each of the above

architectures are shown in Fig. 5. The red lines correspond to specimen responses with the loading edge failure, while the blue lines are for the specimens with mid-gage section failure. Specimens that failed in the gage section (Fig. 4(a)) exhibited an initial linear loading portion followed by a significant load drop when the failure occurred. After this failure, there seems to be a slight residual strength. As shown in Fig. 4 (a), a dominant crack propagates along the yarn undulations around the circumference of the tubular composite. The zigzag nature of the fracture can be attributed to cracks initiating at various locations along the tube circumference and eventually merging along few yarns.

In contrast, the specimens that failed along the loading surface do not exhibit a high load nor a large sudden load drop, but a smaller load drop from a lower peak amplitude and an oscillatory response that extends over a large displacement. This behavior is interpreted as damage initiation along the edge of the specimen in the form of microcracks at a constant load but upon reaching a critical damage level, a smaller load drop occurs. This smaller load drop could be associated with a localized failure in the immediate unit cell(s) or portions of the unit cell(s) at the sample edge. The damage does not extend in the specimen axially, but only over a short distance from the loading surface of about the thickness of a single yarn. The intact material below this thickness resists the load due to the different orientation of the yarn and hence the load has to increase slightly before additional damage is initiated. This process could repeat with progressive failure as the damage moves along the length of the specimen. This would give rise to an oscillatory load-displacement curve which indicates the ability to sustain load-bearing capacity over a large displacement. This behavior of progressive damage initiation and build-up of microcracks along the loading edge continues until the load application is terminated. Continued application of load will cause this region to peel off outward and crumble into powder, but the rest of the specimen remains intact. As shown in Fig. 4(b), there are no observable cracks that penetrated deep into the length of the composite.

Motivated by the observation that microcracks cracks often do not extend beyond one thickness of the yarn, to further understand this behavior, specimens were cut at different lengths (multiple unit-cell lengths as explained in Section 2.1 where the unit cell is outlined in red as in Fig. 1) and compression tests were conducted whose results are

Fig. 5. Load-displacement curves for axial compression testing of the specimens with different architectures. Red lines represent specimens that failed due to edge effect, while the blue lines represent gauge section failure.

discussed in the following for one specific architecture (45° 2-ply biaxial). Fig. 6 shows the load-displacement curves for specimens of length with different number of unit cells under quasi-static compression. All samples were observed to fail at the vicinity of the edge of the specimen. The specimens in Fig. 6 follow a similar trend of an initial elastic response followed by a sharp load drop and then an oscillatory behavior at a significantly lower load level. The initial high stress is attributed to the high strength of the undamaged composite. Damage initiates close to the loading surface and propagates into the specimen along one of the yarn undulations, during which a load drop occurs. After this initial load drop, the intact portion of the composite exhibits a residual strength at a significantly lower load over a sustained period depending on the number of unit cells over the length of the composite specimen. Except for the specimen with a length of 1-unit cell, all other composites exhibited an oscillatory behavior at the same frequency and at relatively the same load. Interestingly, these load oscillations are periodic (with respect to the axial positions) and correspond to the length of about half of the unit cell length. The unit cell length for the 45° 2-ply biaxial architecture is 2.30 mm (see Fig. 1) and the distance between the peaks in the oscillatory part of the curves in Fig. 6 is 1.14 mm ± 0.08 mm. This behavior reflects that damage initiates at a given load first along the loading edge and propagates axially only over the width of a single yarn (half the unit cell) during which the load drops and the damaged material is expelled out while the other yarn (in the opposite orientation) now resists the advancing steel platen as it is undamaged at this displacement or load level. Hence, the load has to increase to initiate damage in the next yarn in the same unit cell. Thus, there are two oscillations per unit cell. This process continues until all the unit cells are fully disintegrated by the loading process. A magnified view of the initial elastic region is shown in the inset.

3.2. Tensile hoop burst

The results from the tensile hoop burst tests for different architectures are summarized in Fig. 7. The 60° 2-ply biaxial architecture exhibited the highest hoop strength of approximately 430 MPa and all others exhibited hoop strength of approximately 250 MPa. The higher strength of the former composite is attributed to the 60° orientation of the yarns, which are more favorably biased towards the circumferential direction, providing more reinforcement in the hoop direction compared
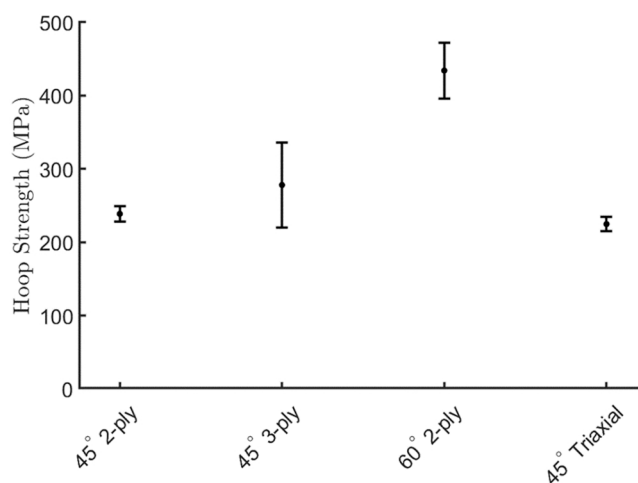

Fig. 7. The hoop burst tensile strength of each SiC_f-SiC_m composite architecture. The error bars are one standard deviation of the data.

to the 45° architectures, all of which exhibited lower strength values. As expected, while the total load increased by adding an additional layer and wall thickness for the 45° 3-ply architecture (vs. 2-ply) the strength was comparable. However, it was observed that the addition of additional axial reinforcement (in the 45° 2-ply triaxial compared to the 45° 2-ply biaxial), did not appear to have a significant impact on the hoop strength. This result implies that it is more effective to have a suitably biased yarn to resist hoop stress than adding a ply or increasing the thickness of the composite.

During the hoop burst tests, it is important to ensure that uniform hoop strain was induced over a certain length of the tube during the elastic loading. To monitor the induced strain, DIC in conjunction with high-speed imaging was implemented on three test specimens from each architecture. A typical result is shown in Fig. 8. It is seen from Fig. 8(a) that in the region where the elastomeric insert is located inside the tubular composite, a uniform hoop strain developed along the length of the tube. Due to the sharp curvature of the tube, the strains on the entire cylindrical surface of the tube could not be captured by the DIC software and by the cameras. With the increase in internal pressure, a highly
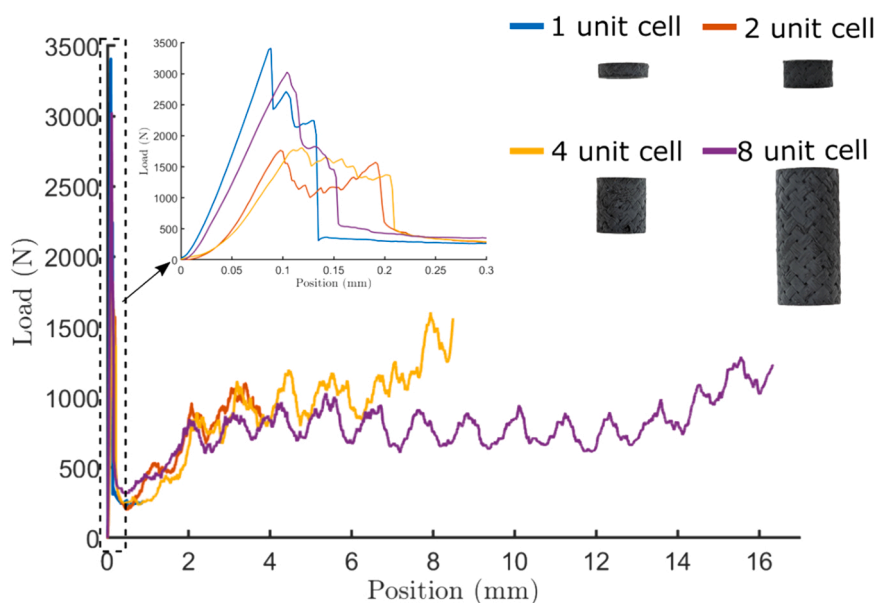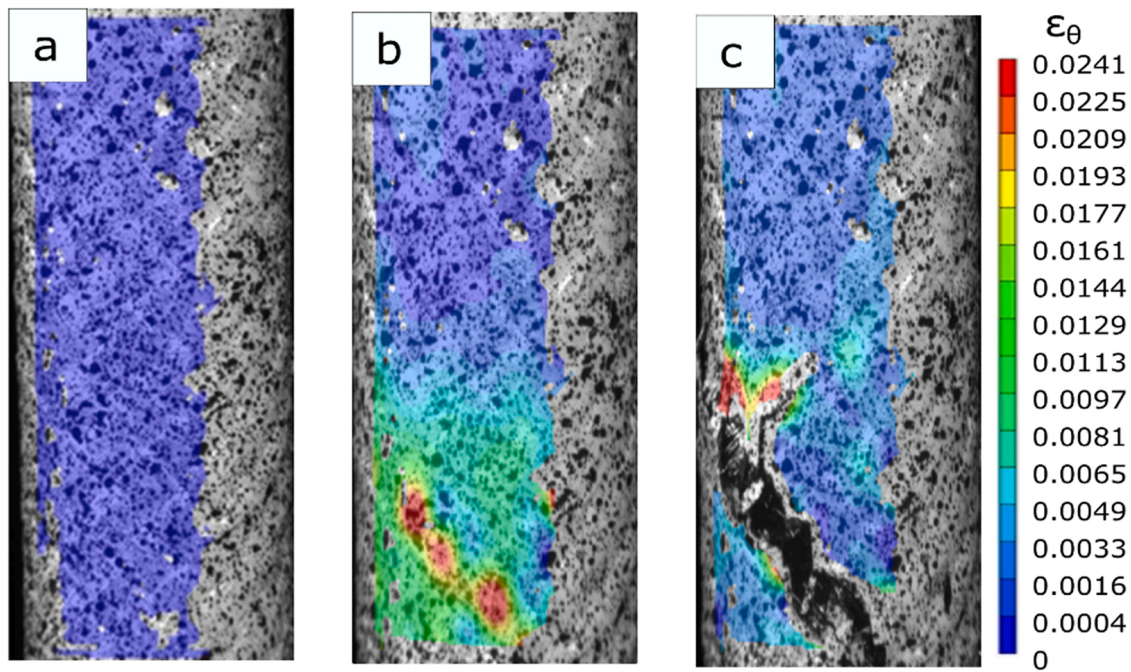

Fig. 6. Axial compression response of 45° 2-ply biaxial the composite with different unit cell length test specimens. The inset reveals the magnified view of the initial portion of the curves.
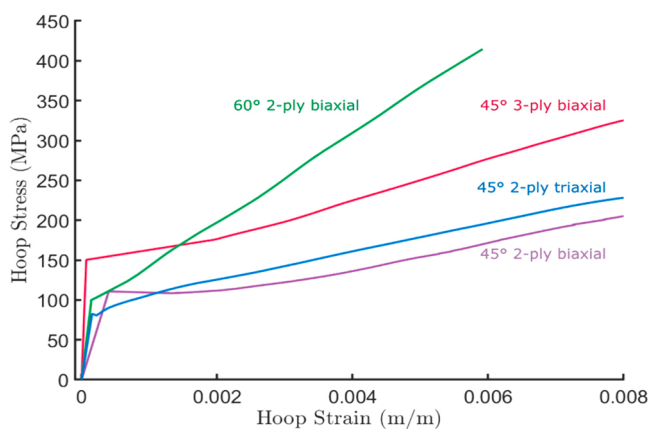
Fig. 8. Sequence of DIC images from a typical hoop burst test: (a) Initial uniform hoop strain over certain length of the composite, (b) a frame just before final fracture showing highly localized increase in strain where fracture is about to occurs, and (c) frame after final fracture.

localized region of strain develops along a yarn as shown in Fig. 8(b). This highly localized region of increased strain is an indication of the location where the final fracture is about to occur which is depicted in Fig. 8(c). This mode of fracture is similar to the one described in the previous axial compressive loading where the initial damage extends only over the width of a yarn and then such microcracks coalesce to form the macroscopic fracture pattern along the inclined yarn as seen in Fig. 4 (a).

Typical hoop stress versus hoop strain curves for each composite architecture are shown in Fig. 9. The hoop stress was calculated as per Eq. (1) at the outer diameter and the hoop strain was averaged over the DIC region (Fig. 8) where the elastomeric insert is located within the composite. Each composite exhibited an initial elastic region followed by an inelastic region that is typical of fiber-reinforced ceramic matrix composites [24]. Interestingly, the proportional limit stress (PLS) for all the 2-ply architectures is similar, at approximately 90 MPa, while the 45° 3-ply biaxial architecture had the highest PLS of 150 MPa and a higher stiffness due to the increased wall thickness. Matrix microcracking begins at the onset of PLS and the tubular composites begin to

exhibit inelastic deformation as the cracks start to grow [25]. Significant strain hardening-like behavior is exhibited by all the composites during this microcrack growth phase with the 60° 2-ply biaxial composite revealing the highest additional loading capacity due to its circumferentially biased yarns. Typically, the composite matrix and level of densification has a strong impact on the PLS. However, these results indicate that for composites with similar levels of matrix densification, an important factor affecting the PLS is the thickness of the composite. The ultimate tensile strength (UTS) is dictated by the reinforcing fiber and the braiding angle of the composite.

The failure modes for the hoop tensile loading in each architecture are shown in Fig. 10. All architectures exhibited the pseudo-ductile behavior and failed gracefully. Interestingly, all architectures containing 2-plies displayed a similar failure pattern, where failure corresponded to the tensile stress direction, while the 45° 3-ply biaxial composite failure propagation was along the direction of the fiber architecture. The former three architectures exhibited a crack that runs along the length of the composite in the gage section (where the elastomeric insert originally was). This is the typical mode of failure for brittle materials due to hoop loading [12]. However, for the 45° 3-ply biaxial, the crack runs at a 45° angle along the length of a single yarn instead. To get a better understanding of the local failure mode for this architecture, a high-speed camera was utilized to capture the evolution of damage during the test. Various keyframes from the hoop tensile burst test are presented in Fig. 11. Note that initially, micro-cracks spanning the width of a yarn and parallel to the vertical axis of the tube form at various locations along one of the yarns, and upon reaching a critical density, a macroscopic crack propagates along the same yarn. This fracture process indicates that hoop-dominated failure initiates in each yarn at a microscopic scale and as the load is increased, these cracks coalesce to form a macrocrack, which propagates along the braiding angle of the yarn.

3.3. Flexural testing

The characteristic load-displacement curves during the rotating flexural testing of cylindrical specimens for each architecture are shown in Fig. 12. The oscillations in the curves are an artifact of the cyclical
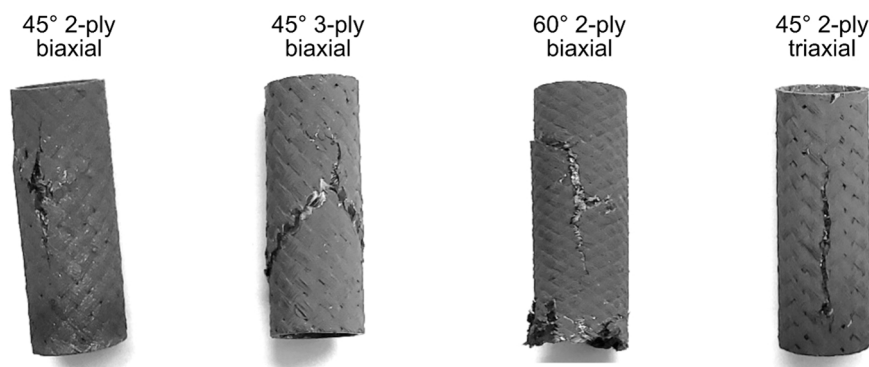

Fig. 9. Representative hoop stress versus hoop strain curves for composite specimens' various architectures.

Fig. 10. Failure modes from the tensile hoop burst tests for each architecture.

Fig. 11. 45° 3-ply biaxial hoop burst test captured using a high-speed camera at different times throughout the test (pristine sample, initial fracture, and highest strength). The red arrows indicate the location of microcracks initiated early during the fracture.
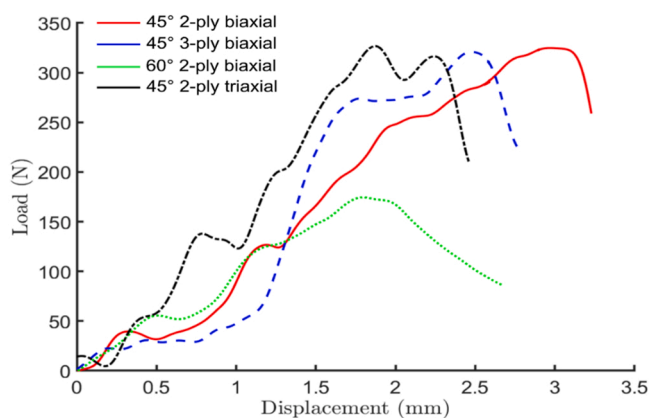

Fig. 12. Characteristic load-displacement curves for each architecture from the rotating flexural test.

loading during the rotating bend test. Because the cylindrical surfaces of the SiC$_f$-SiC$_m$ composites are fairly rough (see Fig. 1) due to the braiding process, the roller surfaces temporarily lose contact with the sample as they rotate and encounter a trough between the braids. Thus, there is a temporary slight drop in load. Due to the highly uneven nature of surface roughness, the contact (or the loss of contact) of the rollers with the specimen surface at all the contact points is not synchronized and hence the appearance of these oscillations is random for each test. This cyclical load and unload results in the fluctuations in the curves of the load-displacement response.

Because of the oscillations exhibited in the load-displacement curves, it is difficult to draw conclusions of the elasticity and plasticity behavior of the specimens. However, the peak load obtained can still be used to quantify the flexural strength of the materials and thus the overall load-

bearing capacity. The results of the flexural strength are summarized in Fig. 13. All of the 45° braided architectures have a similar flexural strength of in the range of approximately 135–145 MPa, while the 60° braided composite is significantly weaker at 55 MPa. By adding an extra ply, there is a slight increase in strength between the 45° 2-ply biaxial and the 45° 3-ply biaxial architectures and a significant decrease in the variability of the strength of the composite. The hoop-biased 60° 2-ply biaxial architecture is significantly weaker than the 45° architectures. This is because the yarns in the 60° 2-ply biaxial architecture are not reinforcing in the induced tensile loading direction (i.e., along the length of the tube) for this flexural stress state. Also, the 45° 2-ply triaxial
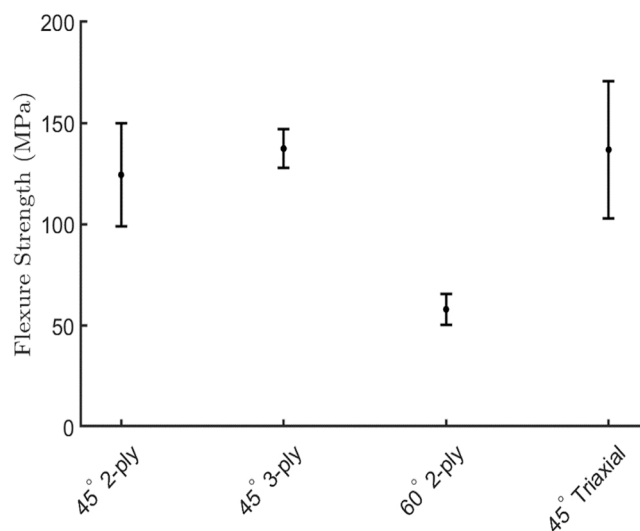

Fig. 13. The flexure strength of each SiC$_f$-SiC$_m$ composite architecture. The error bars are one standard deviation of the data.

composite exhibited the highest strength because the axial yarns align with the tensile stress state in this flexural loading mode and hence provide the best resistance.

The composites tested with the rotating flexural fixture exhibit slightly lower ultimate strengths when compared with samples tested using conventional 4-point flexure fixtures. Bumgardner et al. reported for a similar SiC_f-SiC_m architecture (50° 3-ply biaxial diamond pattern), when tested with a conventional 4-point flexure, the strength values of approximately 200 MPa [26]. As expected, this value is slightly higher than the currently reported value for the 45° biaxial plain-woven architecture from the current study at approximately 140 MPa. Also, the 45° has a reinforcing fiber slightly more aligned along the axial loading direction than the 50° architecture studied in [26] and would therefore be expected to have higher strength. This further highlights this difference between the two values and can be attributed to the critical flaw having a higher potential to be activated using the rotating flexure test, resulting in a lower ultimate strength value.

3.4. Discussions

From all the above experimental studies in various loading modes and failure characterization, it is shown that the architecture of the composites does play a significant role in the strength and the failure modes exhibited by the SiC_f-SiC_m composites. In axial compression, the 45° biaxial architecture provides the highest axial compression load-bearing capacity due to the axial orientation of the yarns. The difference between a 2-ply and 3-ply structure is negligible, and the 45° 2-ply composite has comparable axial strength to the 3-ply structure (only 5% difference in strength, see Table 2). However, all the composites suffer from an increased propensity for crack initiation from the cut surfaces. The loading surface quality definitely affects the load-bearing capacity of these composites under axial loading. Higher quality cut surface results in higher axial strength. Beyond specimen preparation for mechanical testing, this shows that care in surface preparation is important when implementing these composites as parts in specific applications, in order to avoid increased risk of crack initiation.

From Figs. 7 and 13, the 60° 2-ply biaxial composite exhibits the highest hoop strength but the lowest flexural strength compared to all other composites. The hoop-biased yarns at 60° are favorable for resisting hoop stresses but not favorable for resisting tensile load arising from flexural loading. However, the remaining three composites, although different in architectures, show similar strengths under both hoop and flexural loads. From the results provided in Fig. 7, it is concluded that it is better to bias the yarns to increase the hoop strength rather than increase the number of plies in a tube which has the disadvantage of increased material cost and weight of the tube without significant improvement in strength. For an application that requires high strength (rather than overall load-carrying capacity), optimization of fiber architecture can be used to tailor the composite to the application without excessive material use. Even for flexural loading, the extra ply in the 45° 3-ply biaxial composite does not provide any significant improvement in strength (see Fig. 13). These observations and conclusions can be carefully assessed while designing the composites for specific desired applications.

Regardless of loading type (or stress state), all the composites and architectures show one common damage feature for these loading conditions: microscopically, cracks always initiate parallel to the axis on the circumference of the tube and cut the inclined yarns over their width. This mechanism is clearly evident in Fig. 4 for axial loading, and in Fig. 11 for hoop burst test. Eventually, these cracks coalesce to form macroscopic cracks along the yarn orientation. This mode of microcracking also gives rise to oscillatory load-displacement response in axial loading (Fig. 5) and contributes to eventual tube burst either along the length of the tube or at an angle along the yarns, as in Fig. 10 in hoop burst tests. A similar fracture mechanism also appears to be operative during the flexural loading. Thus, despite the differences in the weave architecture of the composites and the loading mode, the fundamental mechanism of damage initiation and growth appears to be the same in all the SiC_f-SiC_m composites considered in this study. Such fundamental understanding is essential for the development of mechanistic models to capture the mechanical response of these composites under complex loading conditions such as those encountered during operation in nuclear applications and/or under loss of coolant accident (LOCA) and other accident scenarios.

4. Conclusions

The failure behavior of the SiC_f-SiC_m tubular composite tubes with four different architectures was investigated under uniaxial compression, tensile hoop, and rotating flexural loads. For quasi-static compressive load, composites with more fibers aligned in the loading direction exhibited higher strengths when failure occurred in the gage section. In contrast, when edge failure occurred the tube architecture did not have a significant impact on the compressive strength. The dominant fracture mode consisted of cracks initiating at discrete locations within one yarn length and eventually coalescing to form a macrocrack. Crack propagation occurred in two steps within each unit cell corresponding to the fracture in the two yarns of opposite orientation. This process was reflected as two oscillations in the load-displacement curves. The residual strength of the damaged specimen remained fairly constant regardless of the number of unit cells.

The hoop burst test results indicated that braiding angle was the most dominant factor influencing the increasing load-carrying capacity beyond the PLS and the failure in this loading mode. The 60° architecture had a much stiffer response beyond the PLS (surviving increasing stress relative to increased strain) as well as a higher hoop strength compared to all the 45° architectures due to the favorable yarn bias to this stress state.

Similar to the hoop burst, the braiding angle was once again found to be the most significant factor affecting the flexure strength of the composites. The 45° architectures exhibited higher strength when compared to the 60° architecture.

CRediT authorship contribution statement

James Nance: Methodology, Validation, Investigation, Writing – original draft, Visualization. **Ghatu Subhash:** Conceptualization, Supervision, Writing – review & editing. **Bhavani Sankar**: Conceptualization, Supervision. **Nam-Ho Kim:** Conceptualization, Supervision. **Christian Deck:** Conceptualization, Supervision. **Sarah Oswald**: Methodology, Investigation.

Declaration of Competing Interest

The authors declare that they have no known competing financial interests or personal relationships that could have appeared to influence the work reported in this paper.

Data Availability

The data that has been used is confidential.

References

[1] S.S. Raiman, C. Ang, P. Doyle, K.A. Terrani, Hydrothermal corrosion of SiC materials for accident tolerant fuel cladding with and without mitigation coatings, Miner. Met. Mater. Ser. (2019) 1475–1483, https://doi.org/10.1007/978-3-030-04639-2_98.

[2] G.N. Morscher, Tensile creep and rupture of 2D-woven SiC/SiC composites for high temperature applications, J. Eur. Ceram. Soc. 30 (2010) 2209–2221, https://doi.org/10.1016/j.jeurceramsoc.2010.01.030.

[3] K.A. Terrani, Accident tolerant fuel cladding development: Promise, status, and challenges, J. Nucl. Mater. 501 (2018) 13–30, https://doi.org/10.1016/j.jnucmat.2017.12.043.

[4] Y. Katoh, K. Ozawa, C. Shih, T. Nozawa, R.J. Shinavski, A. Hasegawa, L.L. Snead, Continuous SiC fiber, CVI SiC matrix composites for nuclear applications: Properties and irradiation effects, J. Nucl. Mater. 448 (2014) 448–476, https://doi.org/10.1016/j.jnucmat.2013.06.040.

[5] G.N. Morscher, J.A. Dicarlo, J.D. Kiser, H.M. Yun, Effects of fiber architecture on matrix cracking for melt-infiltrated SiC/SiC Composites, Int. J. Appl. Ceram. Technol. 7 (2010) 276–290, https://doi.org/10.1111/j.1744-7402.2009.02422.x.

[6] B. Yang, X. Zhou, Y. Chai, Mechanical properties of SiCf/SiC composites with PyC and the BN interface, Ceram. Int. 41 (2015) 7185–7190, https://doi.org/10.1016/j.ceramint.2015.02.041.

[7] J.S. Park, H. Nishimura, D. Hayasaka, J.H. Yu, H. Kishimoto, A. Kohyama, Fabrication of short SiC fiber reinforced SiC matrix composites with high fiber volume fraction, Fusion Eng. Des. 109–111 (2016) 1174–1178, https://doi.org/10.1016/j.fusengdes.2015.12.060.

[8] C.P. Deck, H.E. Khalifa, B. Sammuli, T. Hilsabeck, C.A. Back, Fabrication of SiC-SiC composites for fuel cladding in advanced reactor designs, Prog. Nucl. Energy 57 (2012) 38–45, https://doi.org/10.1016/j.pnucene.2011.10.002.

[9] G.M. Jacobsen, J.D. Stone, H.E. Khalifa, C.P. Deck, C.A. Back, Investigation of the C-ring test for measuring hoop tensile strength of nuclear grade ceramic composites, J. Nucl. Mater. 452 (2014) 125–132, https://doi.org/10.1016/j.jnucmat.2014.05.002.

[10] C.H. Bumgardner, F.M. Heim, D.C. Roache, A. Jarama, P. Xu, R. Lu, E.J. Lahoda, B.P. Croom, C.P. Deck, X. Li, Unveiling hermetic failure of ceramic tubes by digital image correlation and acoustic emission, J. Am. Ceram. Soc. 103 (2020) 2146–2159, https://doi.org/10.1111/jace.16854.

[11] E. Rohmer, E. Martin, C. Lorrette, Mechanical properties of SiC/SiC braided tubes for fuel cladding, J. Nucl. Mater. 453 (2014) 16–21, https://doi.org/10.1016/j.jnucmat.2014.06.035.

[12] K. Shapovalov, G.M. Jacobsen, L. Alva, N. Truesdale, C.P. Deck, X. Huang, Strength of SiCf-SiCm composite tube under uniaxial and multiaxial loading, J. Nucl. Mater. 500 (2018) 280–294, https://doi.org/10.1016/j.jnucmat.2018.01.001.

[13] ASTM C1424 -10, Standard test method for monotonic compressive strength of advanced ceramics at ambient temperature, ASTM Int. 08 (2010) 1–13, https://doi.org/10.1520/C1424-15R19.ization.

[14] F. Schmid, K. Schmid, C.P. Khattak, C. Systems, C. Street, D.C. Harris, High temperature compression and ring-on-ring testing of sapphire, 3705 (n.d.) 17–27.

[15] G. Singh, R. Sweet, N.R. Brown, B.D. Wirth, Y. Katoh, K. Terrani, Parametric evaluation of SiC/SiC composite cladding with UO2 fuel for LWR applications: fuel rod interactions and impact of nonuniform power profile in fuel rod, J. Nucl. Mater. 499 (2018) 155–167, https://doi.org/10.1016/j.jnucmat.2017.10.059.

[16] M. Ben-Belgacem, V. Richet, K.A. Terrani, Y. Katoh, L.L. Snead, Thermo-mechanical analysis of LWR SiC/SiC composite cladding, J. Nucl. Mater. 447 (2014) 125–142, https://doi.org/10.1016/j.jnucmat.2014.01.006.

[17] J.G. Stone, R. Schleicher, C.P. Deck, G.M. Jacobsen, H.E. Khalifa, C.A. Back, Stress analysis and probabilistic assessment of multi-layer SiC-based accident tolerant nuclear fuel cladding, J. Nucl. Mater. 466 (2015) 682–697, https://doi.org/10.1016/j.jnucmat.2015.08.001.

[18] ASTM C1819-15: Standard Test Method for Tensile Hoop Strength of Continuous Fiber-Reinforced Advanced Ceramic Tubular Specimens at Ambient Temperatures Using Elastomeric Insert, 14, 2016, pp. 1–17 doi: 10.1520/C1819-15.posites.

[19] K. Mosley, The stressing for test purposes of materials in tubular form using elastomeric inserts.pdf, Eng. Sci. Div. 196 (1982).

[20] J. Pittarri, G. Subhash, Fracture toughness testing of advanced silicon carbide ceramics using digital image correlation, Dyn. Behav. Mater. Vol. 1 (65) (2015) 207–212, https://doi.org/10.1007/978-3-319-06995-1.

[21] K. Upadhyay, G. Subhash, D. Spearot, Hyperelastic constitutive modeling of hydrogels based on primary deformation modes and validation under 3D stress states, Int. J. Eng. Sci. 154 (2020) 103314, https://doi.org/10.1016/j.ijengsci.2020.103314.

[22] M. MacIsaac, S. Bavdekar, J. Nance, B. Sankar, N.-H. Kim, G. Subhash, A novel rotating flexure-test technique for brittle materials with circular geometries, Exp. Tech. (2022), https://doi.org/10.1007/s40799-022-00565-6.

[23] B. Owens, J. Whitcomb, J. Varghese, Effect of finite thickness and free edges on stresses in plain weave composites, J. Compos. Mater. 44 (2010), https://doi.org/10.1177/0021998309347571.

[24] C.P. Deck, G.M. Jacobsen, J. Sheeder, O. Gutierrez, J. Zhang, J. Stone, H.E. Khalifa, C.A. Back, Characterization of SiC-SiC composites for accident tolerant fuel cladding, J. Nucl. Mater. 466 (2015) 667–681, https://doi.org/10.1016/j.jnucmat.2015.08.020.

[25] J.J. Brennan, Interfacial characterization of a slurry-cast melt-infiltrated SiC/SiC ceramic-matrix composite, Acta Mater. 48 (2000) 4619–4628, https://doi.org/10.1016/S1359-6454(00)00248-2.

[26] C.H. Bumgardner, F.M. Heim, D.C. Roache, A. Jarama, M.C. Price, C.P. Deck, X. Li, Analysis of SiC/SiC composites for energy applications at ambient conditions, J. Am. Ceram. Soc. 104 (2021) 481–491, https://doi.org/10.1111/jace.17462.